Journal of Constructional Steel Research 235 (2025) 109867

Contents lists available at ScienceDirect

Journal of Constructional Steel Research

journal homepage: www.elsevier.com/locate/jcsr

Structural behaviour of demountable tubular column-to-base plate joints with welded studs

Ismael García García [a,b,*], Carlos López-Colina Pérez [b], Miguel Ángel Serrano López [b], Fernando López Gayarre [b], Antolín Lorenzana Ibán [a]

[a] University of Valladolid, Department of Architectural Construction, Geotechnics, Continuum Mechanics and Structures, School of Industrial Engineering, Valladolid 47011, Spain

[b] University of Oviedo, Department of Construction and Manufacturing Engineering, Campus Gijón, 33203, Spain

ARTICLE INFO

Keywords:
Demountable construction
Tubular structures
Welded studs
Bolted connections
Joint characterization
Component method

ABSTRACT

Demountable joints play a key role in enabling structural reuse and sustainable construction. By reducing material waste and facilitating future adaptability, they contribute to more resource-efficient building lifecycles. This study presents a novel demountable column-to-base plate joint for tubular steel structures, designed to enable disassembly and structural reuse in alignment with circular economy principles. The proposed connection, composed of four angle cleats and welded studs, is evaluated through full-scale testing and validated finite element modelling. A validated numerical model was first developed using data from eight experimentally tested joints, achieving good agreement with measured rotational stiffness, with a mean absolute percentage error of 1.87 %. This model was then used to simulate an extended set of 23 configurations to investigate the influence of geometric parameters. Results reveal that wall thickness exerts a structural effect beyond its contribution to the moment of inertia, which may be attributed to local deformation mechanisms or elastic instabilities influencing joint stiffness in slender tubular profiles. When stiffness values are properly scaled, they collapse onto a single trend governed by the slenderness ratio, enabling the derivation of a generalized stiffness decay law for geometrically similar tubular joints. A refined component-based analytical model was also developed, capturing the observed trends and providing conservative estimates with acceptable accuracy. Compared to Eurocode formulations, which exhibit limited predictive capability for this joint typology, the proposed models offer a reliable and practical design tool for demountable tubular steel connections.

1. Introduction

The global energy consumption attributed to buildings, encompassing both residential and commercial sectors, has exhibited a consistent upward trend, achieving percentages ranging from 20 % to 40 % in developed nations [1]. This energy consumption is higher than in other sectors such as industrial and transportation. Furthermore, construction activities account for over half of global resource consumption and yield the largest waste output worldwide. Many research publications have delved into the emissions associated with construction materials across their life cycle stages, encompassing manufacturing, construction, replacement, and end-of-life phases [2].

The conventional linear economic model, typified by the "extract, produce, dispose" paradigm, has been identified as environmentally unsustainable [3]. Consequently, there has been a discernible shift in scholarly attention toward the circular economy (CE) model [4], hailed for its enhanced efficiency and environmental stewardship in economic progression. The CE model endeavors to address environmental concerns such as resource depletion, greenhouse gas emissions, and the management of construction and demolition waste.

Diverging from the linear economy, the CE framework strives to prolong product lifespans and minimize waste through judicious design and material utilization. It entails optimizing end-of-life product handling processes and enhancing the segregation of components and materials to facilitate their recovery via repair, recycling or energy recuperation pathways. Realizing a circular economy in construction necessitates the implementation of designs conducive to efficient materials recovery through disassembly and deconstruction methodologies

* Corresponding author at: University of Valladolid, Department of Architectural Construction, Geotechnics, Continuum Mechanics and Structures, School of Industrial Engineering, Valladolid 47011, Spain.

E-mail address: garciaismael@uva.es (I. García García).

https://doi.org/10.1016/j.jcsr.2025.109867
Received 20 May 2025; Received in revised form 30 July 2025; Accepted 9 August 2025
Available online 16 August 2025

[5]. A design strategy aimed at mitigating the environmental impact in buildings is the concept of Design for Disassembly (DfD) [6,7]. This approach [7,8], focuses on facilitating the disassembly of buildings rather than resorting to demolition. The principal aim of DfD is to enhance material efficiency across the lifecycle of buildings, encompassing both operational and end-of-life phases. This is achieved through a reduction in material consumption, minimisation of waste generation, and promotion of on- and off-site reuse opportunities [9,10].

DfD is acknowledged as a strategy to establish closed material loops [5,11]. Key principles of DfD include detachability, ensuring that components can be separated without damage using detachable connection techniques such as screws or bolts. Furthermore, independence is essential to ensure that parts can be retrieved without compromising the stability of the assembly [12].

Achieving demountable joints in structural frames accounting for hollow-section members poses significant challenges due to the inaccessibility of internal faces for conventional bolting. In particular, bolted joints require openings in the tube walls, which compromise structural integrity by introducing stress concentration effects [13]. To address these limitations, alternative approaches have been proposed. Blind bolts such as Hollo-bolts have been investigated for beam-to-column connections involving tubular columns [14–16]. Other studies have explored the use of intermediate components—channels, angle cleats, stiffeners—to facilitate connections to hollow sections [17–20].

Among demountable solutions, welded threaded studs have emerged as a practical and cost-effective alternative. First proposed by Maquoi [21,22] and later developed by Vandegans et al. [23–25], this technique avoids the need for internal access by welding studs directly to the outer face of the tube. More recently, Neves et al. [26] and Serrano et al. [27,28] have applied this approach to beam-to-column joints, demonstrating promising results for reuse in modular construction.

Despite extensive research on semi-rigid and rigid connections, including end-plate joints [29–32] and angle cleat connections in open-section members [33], the specific configuration involving demountable column-to-base plate joints with angle cleats and welded studs in tubular columns remains largely unexplored. While various models have been proposed to describe the moment–rotation behaviour of extended end plate and angle cleat joints—some accounting for bolt pretension effects [34–36] these studies generally concern beam-to-column joints in non-tubular geometries or focus on non-demountable solutions.

In tubular columns, studies have primarily addressed end-plate joints [37], concrete-filled steel tube columns [16,19,38,39] or welded stud connections in beam-column configurations [26,40,41], yet none have investigated the structural performance of demountable column-to-base plate joints employing welded studs and angle cleats. Moreover, component-based design formulations, as codified in Eurocode 3, have shown limited accuracy when applied to such configurations [42–46], motivating recent proposals for refined stiffness models.

To fill this gap, the present work proposes a novel column-to-base plate joint designed according to circular construction principles, aiming to facilitate disassembly and reuse in low-rise steel buildings. Its structural behaviour—defined in terms of stiffness and resistance—is assessed through a combined experimental, numerical, and analytical approach.

2. Experimental program

Six full-scale column-to-base plate joints with four angle cleats were tested to obtain the actual moment-rotation curve of the joint. From these curves, two key parameters of joint behaviour were determined: the initial rotational stiffness and the moment resistance. Experimental moment-rotation curves were then compared with results from numerical simulations using numerical modelling. Finally, the experimental and numerical curves were utilized to validate the proposed analytical expressions for determining joint stiffness and resistance. These expressions primarily derive from assembling the main identifiable components and characterizing those using simplified equations.

2.1. Column-to-base plate experimental program

Six full-scale column-to-base plate joints were assembled and tested under monotonic load. The joints consisted of a 600 × 600 × 40 mm steel plate connected to RHS and SHS columns, as can be seen in Fig. 1. A group of three specimens (coded as BM1, BM2 and BM3) were made up with a SHS 200 column while another group of other three specimens (BM4, BM5 and BM6) were assembled with a RHS 200 × 150 column. In each group of three specimens, the thickness of the column was varied, forming specimens with tube wall thicknesses of 6 mm, 8 mm, and 10 mm.

Each of the six joints were assembled by connecting the tube to the base plate with four intermediate L-type angle cleats 120 × 80 × 10. Each angle cleat was placed on any of the tube faces, as shown in Fig. 2. To facilitate assembly avoiding interference between cleats at the corners, the angles were shorter than the width of the corresponding tube face, being 180 mm for the 200 mm wide faces and 130 mm for the 150 mm wide faces. Each angle cleat was bolted to the column by its long leg using 4 commercial TR 16 bolts of 10.9 class. The short leg of the angle was bolted to the base plate with 2 welded studs with metric thread, diameter 20 mm, length 35 mm and class K800. The position of the holes in the angle cleat was changed with respect of that used in the beam-column joints [40] for two reasons: a) to avoid interference between two bolts inside the tube at the corners and b) to be able to place the nut inside the tube without colliding with the inner wall of the column face. The dimensions and position of the holes of the angle cleats used in the column-to-base plate specimens can be seen in Fig. 3.

The joint assembly process ensured full demountability in accordance with design-for-disassembly principles. Initially, the long leg of each angle cleat was bolted to the corresponding face of the tubular column using M16 bolts, as illustrated in Fig. 2. Once all four cleats were bolted to the column, the base plate—pre-welded with threaded studs—was positioned such that the short leg of each cleat was brought into direct bearing contact with the plate surface. The connection was then completed by tightening nuts onto the studs, as shown in Fig. 1.

On one side of the base plate was used to test three specimens. Eight studs were welded to the base plate, then four angle cleats were bolted as above described to the plate by the short leg and to the column by the long leg and the specimens formed by SHS 200 tubes (denoted as BM1 to BM3 joints) were tested. Only the last specimen of this batch (BM3) was broken. In order to reuse the same plate, once this first batch of tests was completed, the studs on this face were removed by cutting them and on the opposite side of the plate, the eight studs were welded in the

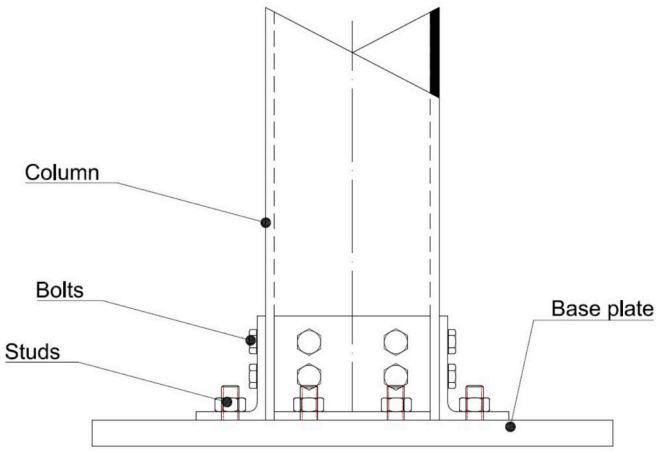

Fig. 1. Sketch of a base plate-to-tubular column joint with unequal-sided angle cleats and welded studs.

Fig. 2. Interior view of a demountable column-to-base plate joint with bolted angle cleats.

positions required by the RHS 200 × 150 tubes (BM4 to BM6 joints). Once again, the first two specimens of the second batch were tested in an elastic regime, obtaining enough data to determine the initial stiffness and allowing the reuse of the studs until the third of the samples (BM6) was tested to failure. In other words, only specimens BM3 and BM6 were broken. The rest of the tests were stopped in linear-elastic behaviour before failure, so that sufficient data was recorded to obtain the initial rotational stiffness. Thus, on one side of the base plate, specimens BM1 to BM3 were tested, while on the other side, were tested the specimens BM4 to BM6. In all the tests the column length was 850 mm. In addition to the above-described tests, in two of the geometries (BM1 and BM2) the lateral angles, located in vertical position, were disconnected, giving rise to another two tests BM1-SA and BM2-SA in which only two angle cleats were supporting the bending moment. Therefore, a total of eight different column-to-base plate geometries were tested, which are presented in Table 1. An example of a joint with the lateral angles disconnected can be seen in Fig. 4.

The geometries of the tested column-to-base plate joints were selected to be directly compatible with previously tested I-beam-to-RHS column joints with welded studs [40], enabling their combined use in the construction of fully demountable moment-resisting steel frames. These complementary connection types, involving hollow-section columns and open-section beams, were designed following principles that facilitate disassembly, structural reuse, and circular construction strategies in steel buildings.

All tests were conducted in a multi-positional reaction frame, where

Table 1
Set-up of the tested column-to-base plate joints.

Joint	Column	No. of angle cleats L 120 × 80 × 10	No. of bolts M16 10.9	No. of studs M20 × 35 K800
BM1	SHS 200.6	4	16	8
BM1-SA	SHS 200.6	2	8	4
BM2	SHS 200.8	4	16	8
BM2-SA	SHS 200.8	2	8	4
BM3	SHS 200.10	4	16	8
BM4	RHS 200.150.6	4	16	8
BM5	RHS 200.150.8	4	16	8
BM6	RHS 200.150.10	4	16	8

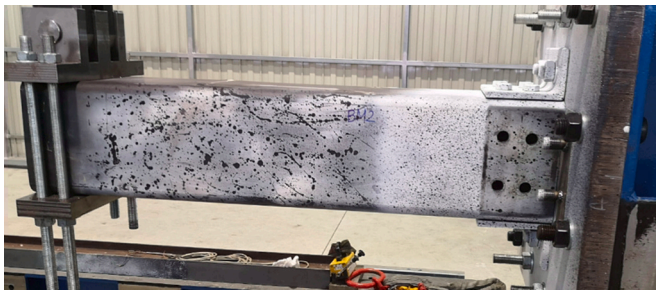

Fig. 4. Column-to-base plate joint with disconnected lateral angle cleats.

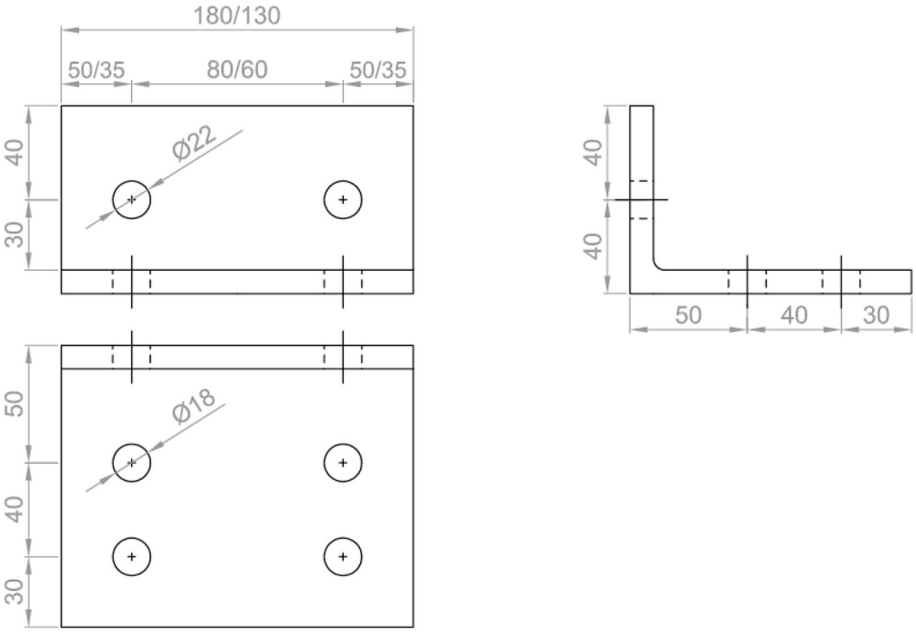

Fig. 3. Geometry of the angle cleats and position of the holes in the column-to-base plate joints.

the column-to-base plate joints were anchored horizontally by fixing the base plate to the support structure, as can be seen in Fig. 5. A vertical force was applied at the free end of the tubular column using a GIB 500-MD2W hydraulic actuator operating under displacement control at a constant rate of 1 mm/min. To monitor deformations, a non-contact digital image correlation (DIC) system—Aramis 5 M (GOM)—was employed. This optical system, synchronized with the actuator load data acquisition, provided full-field displacement measurements over the specimen surface. The joint rotation was determined by computing the difference between the angular rotations of the column and base plate faces. For each component, rotation was estimated as the ratio of the horizontal displacement difference between two vertically aligned points to their vertical separation. The local joint rotation was then calculated as the difference between the column face rotation and the base plate rotation. This approach allowed for a contactless evaluation of moment–rotation behaviour, from which the initial rotational stiffness was obtained by linear regression of the moment–rotation response in the elastic range.

3. Numerical modelling

Detailed numerical simulations of the column- to-base plate joints were carried out by means of the Finite Element software Abaqus. The model consisted of three-dimensional solid elements representing the tube, bolts, angle cleats, and base plate, as can be seen in Fig. 5. To optimise computational resources and reduce calculation time, only half of the union was modelled by exploiting its symmetry. This simplification was justified by the symmetry of geometry, boundary conditions, and loading, and was consistent with the symmetric deformed shape observed experimentally. The modelling of the components employed elasto-plastic isotropic mechanical properties derived from the experimental testing carried out by the authors in a previous study [47] and calibrated using the Abaqus Calibration Tool. The stress vs strain curves of the experimental mechanical properties used in the numerical simulations are shown in Fig. 6. Only the bolts, nuts and washers were modelled with nominal linear elastic properties, with a Young's modulus of 210 GPa and a Poisson ratio of 0,3. This modelling avoids convergence issues associated with localized plastic strains, without significantly affecting the overall joint response [50]. (See Fig. 7.)

The tube was meshed with structured hexahedral elements (C3D8I) with a size of 20 mm and a finer 5 mm mesh in the areas in contact with the angle cleats. The bolts were modelled with three-dimensional, six-node wedge elements (C3D6) and a 3 mm mesh size. The angle cleats were modelled with elasto-plastic isotropic properties using structured hexahedral elements with incompatible modes (C3D8I) [48], with a global 3 mm mesh size and the thickness divided into four elements [49]. The base plate was similarly modelled with hexahedral elements with incompatible modes (C3D8I), with a 10 mm mesh size and a finer 2 mm mesh for the studs. This discretization strategy was confirmed to be sufficient through convergence checks, as further refinement produced negligible variation in joint stiffness.

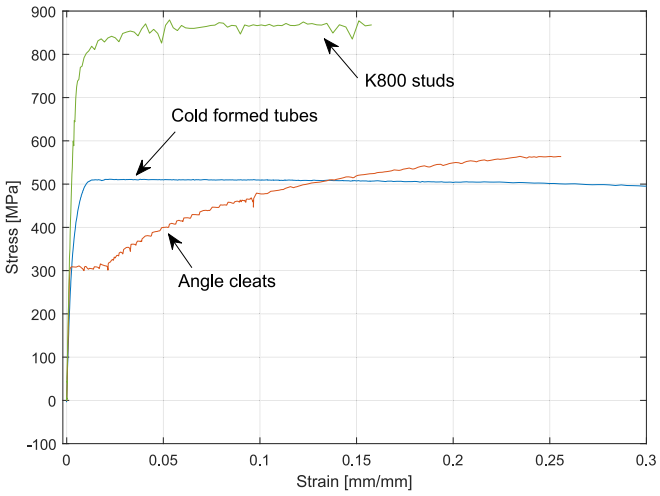

Fig. 6. Stress vs strain curves of the experimental mechanical properties used in the numerical simulations.

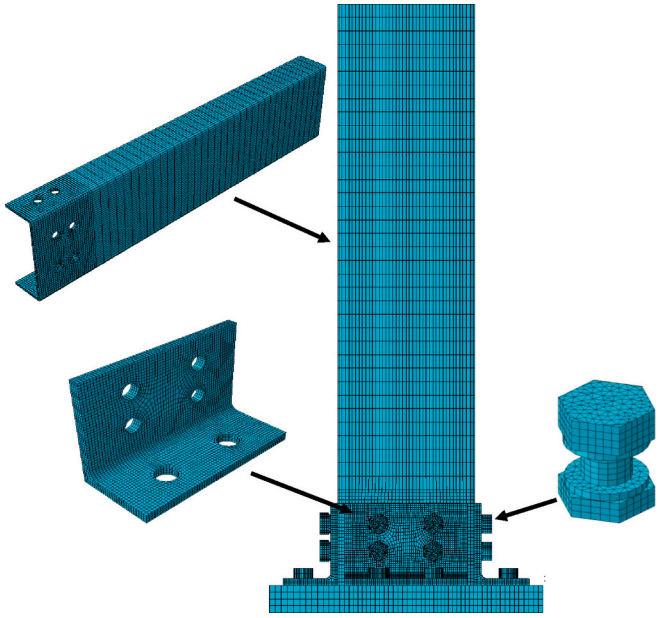

Fig. 7. Detail of the mesh of the column to base plate joint.

The contact interactions between all joint components were modelled using general contact with friction. The normal contact

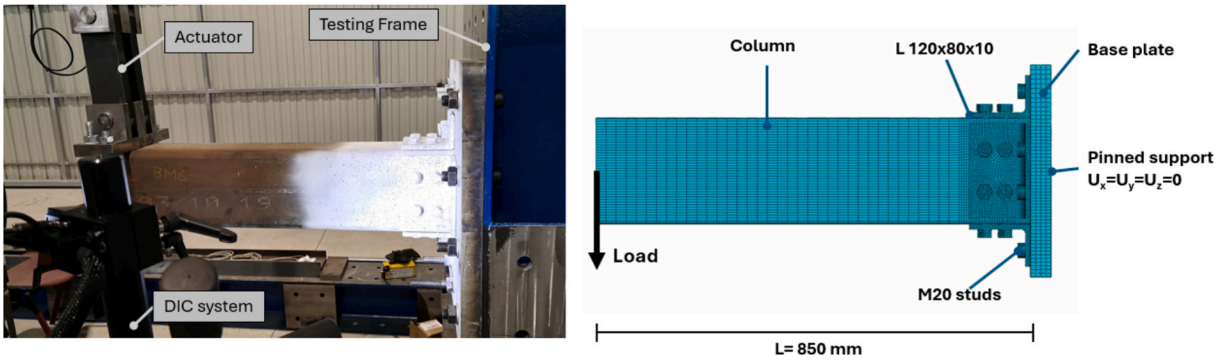

Fig. 5. Experimental test configuration (left) and finite element model for tubular column-to-base plate joints (right).

behaviour was defined as hard contact. The tangential contact behaviour was specified using a penalty formulation with isotropic friction and a coefficient of 0.34, consistent with previous studies [50]. A preload of 58,125 N was applied to the bolts, corresponding to an estimated tightening torque of 190 Nm. Additionally, the studs were preloaded with 28,500 N, which is equivalent to an approximated tightening torque of 110 Nm.

To replicate the experimental conditions, boundary conditions and loading were applied in two sequential analysis steps. In the first step, a pinned support condition was imposed on the back face of the base plate, fully restraining displacements in the x, y, and z directions (i.e., $U_x=U_y=U_z=0$) to simulate the anchorage provided by the testing frame, as shown in Fig. 5. Furthermore, the pretension forces of the bolts and welded studs were applied to reproduce the experimental tightening torques. In the second step, a vertical concentrated load was applied downward over the end face of the tubular column to reproduce the action of the actuator in the physical test.

Fig. 8 shows the experimental setup and a comparison between the deformed shape from the finite element simulation and the experimental response, from which the relative rotations between column and base plate were extracted and subsequently used to plot the numerical moment–rotation curves. The comparison between experimental and numerical moment-rotation curves was conducted for the BM3 and BM6 specimens, which were the two joints tested until failure. This comparison, illustrated in Fig. 9, assess the accuracy of the model predictions. For the BM3 specimen, the analysis, based on 49 data points, yielded the following results: a Mean Absolute Error (MAE) of 0.71, a Mean Squared Error (MSE) of 1.15, a Root Mean Squared Error (RMSE) of 1.07, and a Mean Absolute Percentage Error (MAPE) of 3.02 %. For the BM6 specimen, the analysis, based on 28 data points, showed a MAE of 2.72, a MSE of 8.69, a RMSE of 2.95, and a MAPE of 6.76 %. The less accurate fit observed for the BM6 specimen may be due to slight movements between the parts of the specimen or due to experimental measurement errors, as suggested by the changes in the slope of the experimental moment-rotation curve. However, these results indicate a good level of agreement between the experimental data and the numerical model predictions, suggesting that the numerical model provides a reliable representation of the behaviour of both specimens.

Fig. 10 shows the numerical moment-rotation curves for all the joint geometries tested. The figure displays the curves for the SHS joints on the left and the RHS joints on the right. From the figures, it can be inferred that SHS joints exhibit a more extended linear behaviour compared to RHS joints, mainly attributed to longer angle cleats. Furthermore, for the same column thickness, and throughout the entire moment-rotation curve, SHS joints demonstrate increased stiffness, consistently maintaining higher moments compared to RHS joints. Finally, the effect of column thickness is also revealed, with both RHS and SHS joints showing increased stiffness as column thickness increases.

Fig. 11 shows the effect of the lateral angle cleats in the numerical moment-rotation curves for the RHS joints. The figure illustrates that removing the lateral angle cleats results in a decrease in stiffness, both in the initial slope and throughout the entire curve. For example, for RHS 200 × 6 at 0.03 rad, the moment decreases from approximately 50 kNm to 30 kNm.

For all the tested specimens and the numerical simulations, the initial slope (rotational stiffness) was calculated, and the results are presented in Table 2. Table 2 provides a comparison between the experimental, $S_{j,EXP}$, and numerical, $S_{j,NUM}$, rotational stiffness values for each joint. The ratio of the numerical to experimental stiffness ($S_{j,NUM}/S_{j,EXP}$) is also included. The table shows that the numerical model closely matches the experimental results for all specimens, with stiffness ratios ranging from 0.94 to 1.03 and a MAPE of 1.87 %.

Building upon the finite element model validated through experimental testing, the analysis was extended to include the stiffness characteristics of various column-base plate joint configurations relevant to low-rise buildings. All joints were assembled using SHS square columns and L120 × 80 × 10 angle cleats. Threaded studs (RD M20 K800) connected the angle cleats to the base plate, replicating the test configurations, while 16 mm metric bolts joined the angle cleats to the columns.

To align with the tested joints, the angle cleats were modelled with a length equal to the column width minus 20 mm to simplify assembly and avoid corner collisions. The hole dimensions and edge distances matched those of the experimental specimens, excepting that the bolts and studs were positioned 35 mm from the free end of the angle cleat along its longitudinal axis. The numerically simulated joints, accompanied by their numerically obtained initial stiffness $S_{j,NUM}$, are summarized in Table 3.

3.1. Effect of tube thickness in numerical joint stiffness

The results of the numerical simulation, summarized in Tables 2 and 3, demonstrated that increasing the tube thickness t leads to an increase in the numerical joint stiffness, $S_{j,NUM}$. This behaviour is expected, as an increase in t results in a higher moment of inertia I of the column cross-section, thereby enhancing the flexural stiffness of the member.

To investigate whether the observed increase in stiffness was solely attributable to the increase in I, or if t exerted an additional influence, a comparative regression analysis was carried out. Two linear regression models (Ordinary Least Squares, OLS) using scikit-learn in Python [51] were applied to explain the influence of t on the joint's stiffness. The first used only l as predictor, while the second included both I and t. The inclusion of t improved the model fit from $R^2 = 0.9316$ to $R^2 = 0.9454$, suggesting that tube thickness contributes explanatory power beyond its effect on I.

Further analysis was performed by plotting the normalized stiffness $S_{j,NUM}/I$, as shown in Fig. 12. The distributions reveal that thinner tubes tend to exhibit higher normalized stiffness. This can be attributed to the fact that I increases more rapidly than $S_{j,NUM}$ with increasing t, leading to a decreasing trend in $S_{j,NUM}/I$, i.e. the ratio $S_{j,NUM}/I$ tends to decrease as t increases. Fig. 13 complements this observation by plotting the normalized stiffness against the slenderness ratio h/t, where h is the cross-sectional tube depth. A decreasing trend is observed, with higher h/t ratios associated to thinner tube walls showing lower normalized stiffness, reinforcing the view that wall slenderness influences joint flexibility.

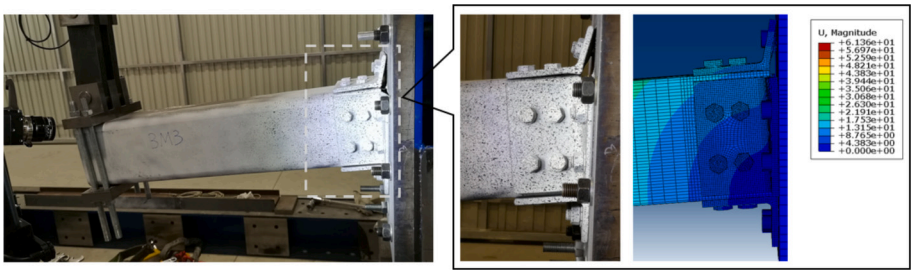

Fig. 8. Experimental setup and detail of the comparison between the deformed shape from the FE simulation and the experimental response.

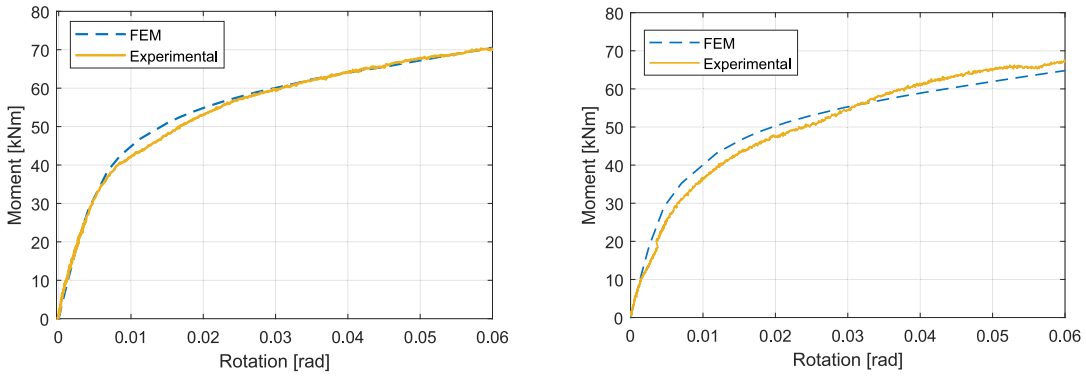

Fig. 9. Numerical and experimental moment-rotation curves for the BM3 (left) and BM6 (right) specimens.

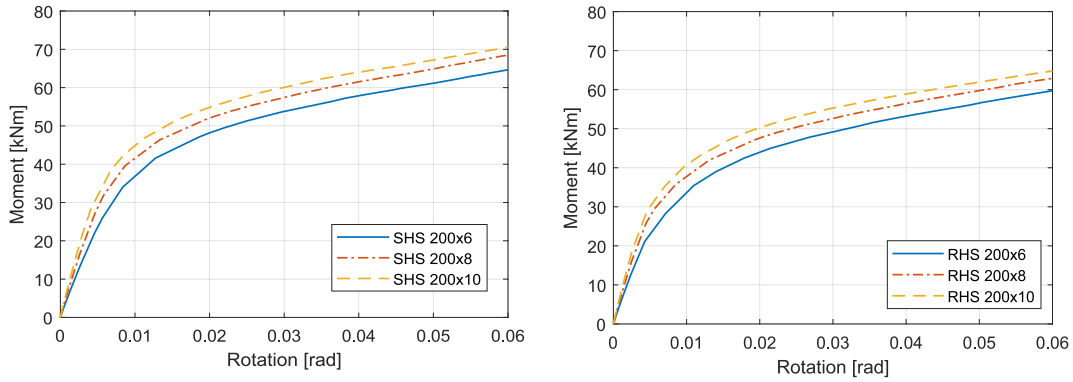

Fig. 10. Numerical moment-rotation curves for the SHS and RHS joints.

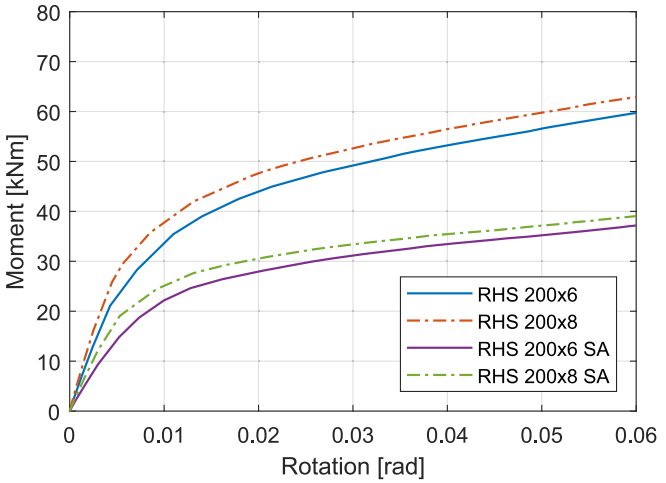

Fig. 11. Effect of the lateral angle cleats in the numerical moment-rotation curves for the RHS joints.

To further explore the dependence of joint stiffness on geometric parameters, two regression techniques were applied: Lasso regression and symbolic regression using the PySR library [52]. The Lasso model [51], trained on polynomial expansions up to the third order of the geometric variables t, h, and z achieved a high predictive accuracy (R^2 = 0.9734, see Fig. 14). The resulting expression is shown in eq. 1 and retained only high-order interaction terms involving t and h, such as $t{\cdot}h^2$, and h^3, reinforcing the idea that the tube thickness t influences stiffness not fully captured by its effect on I.

$$S_{j,Lasso} = 7047{\cdot}\left(t{\cdot}h^2\right) + 627.3{\cdot}h^3 + 3.215{\cdot}10^8 \quad (1)$$

Table 2
Experimental rotational stiffness ($S_{j,EXP}$) and numerical rotational stiffness ($S_{j,NUM}$) of the column-to base plate tested joints.

Joint	$S_{j,NUM}$ [kNm/rad]	$S_{j,EXP}$ [kNm/rad]	$S_{j,NUM}$/ $S_{j,EXP}$
BM1	4588	4567	1,00
BM1-SA	3494	3677	0,95
BM2	5787	5979	0,97
BM2-SA	4192	4391	0,95
BM3	6875	6924	0,99
BM4	4882	5181	0,94
BM5	5838	5792	1,01
BM6	6204	6022	1,03

Table 3
Geometry and numerical stiffness ($S_{j,NUM}$) of the numerically-modelled column-to-base plate joints.

Joint	Column SHS	Thickness of the column [mm]	$S_{j,NUM}$ [kNm/rad]
FEPC01	120	6	1918
FEPC02	120	8	2174
FEPC03	120	10	2494
FEPC04	140	6	2855
FEPC05	140	8	3594
FEPC06	140	10	3747
FEPC07	160	6	3908
FEPC08	160	8	4436
FEPC09	160	10	4789
FEPC10	175	6	4758
FEPC11	175	8	5520
FEPC12	175	10	5741
FEPC13	180	6	5171
FEPC14	180	8	5634
FEPC15	180	10	6012

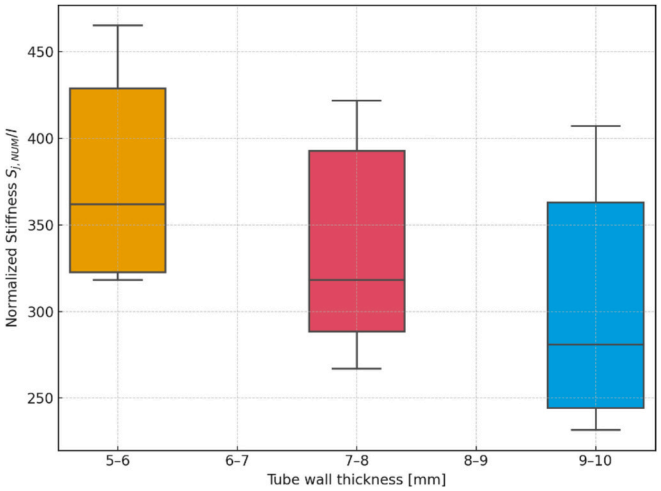

Fig. 12. Effect of the tube wall thickness in the normalized stiffness $S_{j,NUM}$ /I.

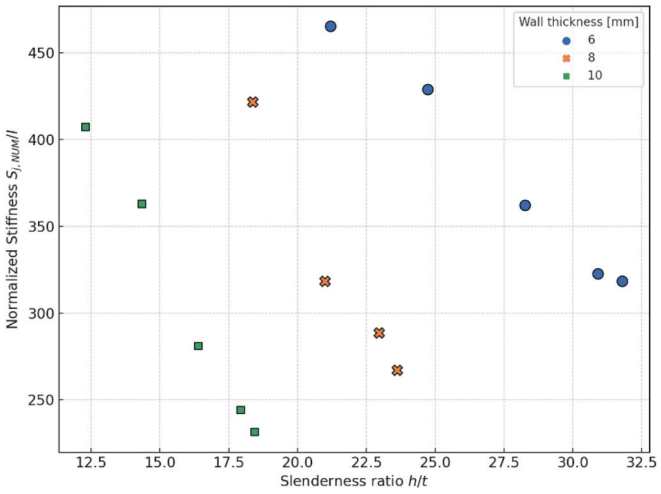

Fig. 13. Effect of slenderness ratio h / t in the normalized stiffness $S_{j,NUM}$ /I.

Symbolic regression with PySR produced an even more accurate model (R^2 of 0.9967, Fig. 14) yielding a compact nonlinear expression that bypassed the use of I and relied directly on t and h, as shown in eq. 2.

$$S_{j,PySR} = h\cdot\left(7.0157\cdot10^{7} - \left(7.2134\cdot10^{7}/t\right) - 5.217\cdot10^{9}\right) \quad (2)$$

3.1.1. Discussion

The results demonstrate that although an increase in tube thickness t enhances the numerical joint stiffness ($S_{j,NUM}$), this effect is not fully explained by the corresponding increase in moment of inertia I. The improved fit of the regression model when both I and t are included as predictors (from $R^2 = 0.9316$ to $R^2 = 0.9454$) suggests that t provides explanatory value beyond its contribution to I. This observation is further supported by the normalized stiffness analysis: both the boxplot of $S_{j,NUM}/I$ and its trend with respect to the slenderness ratio (h/t) reveal that local deformation effects, which are not captured by I, become increasingly significant as t decreases.

Additionally, both Lasso and symbolic regression models yielded accurate empirical expressions where the wall thickness t appears explicitly and plays a dominant role. Symbolic regression produced a compact, highly accurate expression that omitted I altogether, relying instead on nonlinear terms involving h and 1/t. These findings indicate that joint stiffness is governed not only by global section properties like the moment of inertia, but also by local geometric features associated with wall slenderness. As a result, design approaches based exclusively on I may fail to capture stiffness variations arising from changes in wall thickness—particularly in slender tubular profiles—as t is expected to influence local deformation mechanisms, such as face flexibility and cleat–tube interaction, which are not reflected in the moment of inertia. However, it should be noted that the empirical expressions were derived under specific conditions —namely the geometry of the tubular columns, the number and arrangement of angle cleats, the bolt layout, bending-dominated loading, preloaded bolts, etc.— and are valid within this context.

3.2. Decay law and scalability of effective rotational stiffness

The initial analysis of $S_{j,NUM}$ /I as a function of the slenderness ratio h/t showed in Fig. 13, revealed strong dependence on wall thickness t, with the data forming separated curves for the different tube sizes. However, upon scaling the normalized stiffness by t^2, the results from all geometries collapsed onto a single master curve governed by h/t, as

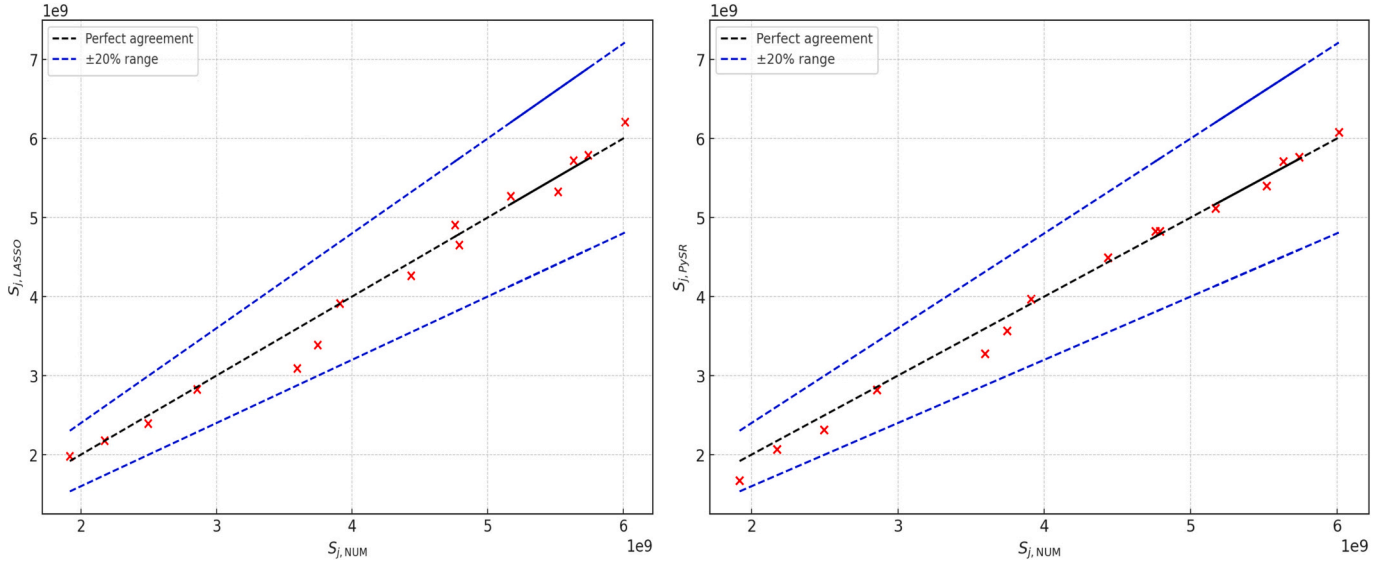

Fig. 14. Assessment of the Lasso model and the symbolic regression model with numerical results.

shown in Fig. 15. This transformation reveals a functional relationship between the scaled stiffness and wall slenderness. This observation provides the basis for defining an effective stiffness parameter that integrates both global flexural stiffness and local elastic instabilities as introduced in Eq. (3):

$$S_{eff} = \frac{S_{j,NUM} \cdot t^2}{I} \tag{3}$$

where $S_{j,NUM}$ is the numerically obtained initial rotational stiffness, t is the wall thickness of the tube, and I is the cross-sectional moment of inertia. This parameter captures the effective joint stiffness normalized with respect to the section's flexural rigidity and scaled by the square of the wall thickness. The influence of the angle cleats is implicitly included in this formulation, as their length scales with the section depth h, contributing to the overall stiffness.

The variation of S_{eff} with respect to h/t, obtained from the numerical results and shown in Fig. 15, indicates a progressive reduction of joint stiffness as the wall slenderness of the tube increases. While this behaviour is primarily attributed to geometric softening mechanisms such as local wall flexibility and incipient elastic buckling, it may also be influenced by the increasing rigidity of the angle cleats, whose length scales with the section depth. The relationship between S_{eff} and h/t was approximated using the power-law decay expression showed in eq. 4.

$$S_{eff} = a\left(\frac{h}{t}\right)^{-m} \tag{4}$$

where a and m are regression coefficients obtained from fitting the numerical dataset. As can be seen in the figure, the model captures the trend across the analysed configurations with an R^2 of 0,9907, providing a compact representation of the stiffness degradation when increasing slenderness.

The identification of this scaling behaviour enables extrapolation of joint stiffness across tubular sections of different sizes, provided that geometric similarity is preserved. In particular, for two sections with the same h/t ratio, the rotational stiffness $S_{j,NUM,2}$ of one configuration can be derived from a known reference $S_{j,NUM,1}$ using the following expression:

$$S_{j,NUM,2} = S_{j,NUM,1} \cdot \left(\frac{I_2}{I_1}\right) \cdot \left(\frac{t_1}{t_2}\right)^2 \tag{5}$$

This relation enables the extrapolation of stiffness values across tubes of different sizes but with identical slenderness ratios, facilitating the use of prototype tests or simulations for design optimization. The applicability of this stiffness extrapolation is valid under conditions of geometric similarity—particularly in terms of cleat proportions, connection layout, number of angle cleats, and stud placement relative to the section depth—as well as identical mechanical properties, loading type, and boundary conditions.

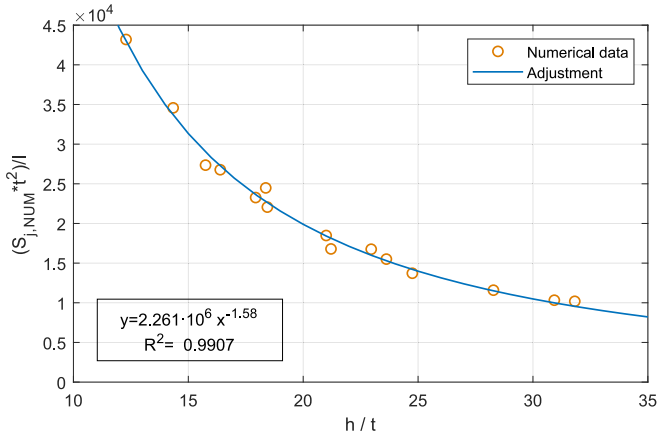

Fig. 15. Effect of slenderness ratio in effective joint stiffness.

4. Analytical modelling of the column-to-base plate joint stiffness

In general, any typical connection configuration can be idealised as an assemblage of uniaxial springs following the component-based method [53,54]. This section assesses an analytical model utilizing the component method to estimate the initial rotational stiffness of the proposed column-to-base plate joints. The subsequent section compares these results to evaluate the agreement between the analytical and numerical rotational stiffness with the experimental values.

4.1. Model of springs

The analytical model of springs based on the component method for the estimation of the rotational stiffness of the proposed column-to-base plate joints is an adaptation of the EC3–1-8 model for end-plate joints with two or more bolt-rows in tension. In joints with two or more bolt-rows subjected to tension, the basic components related to these bolt-rows can be idealised by a single equivalent stiffness coefficient k_{eq}, that can be obtained from (6)

$$k_{eq} = \frac{\sum k_{eff,j} \bullet h_j}{z_{eq}} \tag{6}$$

Where $k_{eff,j}$ is the effective stiffness coefficient for bolt-row '*j*' which can be obtained with the eq. (7), $k_{i,j}$ is the stiffness coefficient representing component '*i*' relative to bolt-row '*j*', h_j is the distance between bolt-row '*j*' and the centre of compression and z_{eq} is the equivalent lever arm that can be determined from eq. (8).

$$k_{eff,j} = \frac{1}{\sum \frac{1}{k_{i,j}}} \tag{7}$$

$$z_{eq} = \frac{\sum k_{eff,j} \bullet h_j^2}{\sum k_{eff,j} \bullet h_j} \tag{8}$$

In this work, the joints were modelled considering three basic components. The basic components considered in the analytical model where the component angle cleat in bending (k_6, following the nomenclature proposed in the Eurocode 3), the studs in tension (k_{10}) and bolts in bearing (k_{12}). The stiffness coefficients corresponding to the basic component bolts in shear (k_{11}) where supposed equal to infinite, following the EC3–1-8 recommendations for preloaded bolts.

4.1.1. Component angle cleat in bending

The stiffness coefficient of the angle cleats in bending, k_6, can be evaluated according to eq. (4), by means of the equivalent T-stub procedure proposed by Faella [54], where the coefficient ψ, accounting for preloading effects, is given by eq. (5), b_{eff} can be calculated according to Table 4, t_l is the thickness of the considered angle cleat, m is the distance between the axis of the stud in tension and the beginning of the radius of curvature of the angle cleat and γ is defined in (6). L_1 is the length of the

Table 4
Effective width of the equivalent T-stubs.

Bolt row	Effective width
Top angle	$b_{eff} = min\left\{d_h + 2m; \frac{d_h}{2} + m + \frac{w}{2}; \frac{b_l}{2}; e_x + \frac{d_h}{2} + m\right\}$
Inner bolt row of web angle	$b_{eff} = min\{d_h + 2m; p\}$
End bolt row of web angle	$b_{eff} = min\left\{d_h + 2m; \frac{d_h}{2} + m + \frac{p}{2}; e_x + \frac{p}{2}; e_x + \frac{d_h}{2} + m\right\}$

Notation: d_h is the stud head diameter; *w* is the distance between two studs/bolts row of a top angle; b_l is the length of the angle cleat; p is the distance between two studs/bolts row of a web angle.

short leg of the angle, measured from the inside face of the column to the axis of the first bolt connecting the angle to the base plate. L_2 is the length of the long leg of the angle, measured from the base plate to the axis of the first bolt connecting the angle to the column.

$$k_6 = \psi \cdot \frac{0.5 \bullet b_{eff} \bullet t_l^3}{m^3} \cdot \left(\frac{4 \cdot \gamma}{4 \cdot \gamma + 3} \right) \tag{9}$$

$$\psi = 0.57 \cdot \left(\frac{t_l^3}{d_h \sqrt{\frac{m}{d_h}}} \right)^{-1.28} \tag{10}$$

$$\gamma = \frac{I_2 / L_2}{I_1 / L_1} \tag{11}$$

4.1.2. Component studs in tension

The stiffness coefficient of the studs in tension, k_{10}, has been estimated in concordance with eq. (7), used in EC3 for bolts in tension, where A_s is the reduced area of the stud, and L_s is the length of the stud subjected to tension, taken as the thickness of the angle cleat plus the washer and half the height of the nut.

$$k_{10} = \frac{1.6 \bullet A_s}{L_s} \tag{12}$$

4.1.3. Component bolts in bearing

The stiffness coefficient of the bolts in bearing, k_{12}, has been adapted from the proposed in EC3. Eq. (8) shows the analytical approximation, where e_b is the distance from the bolt-row to the free edge of the plate in the direction of load transfer; k_b is as defined in eqs. (9 to 11), k_t is as defined in eq. (12), d is the diameter of the hole; f_u is the ultimate tensile strength of the steel on which the bolt bears; p_b is the spacing of the bolt-rows in the direction of load transfer and t_i is the thickness of the analysed plate.

$$k_{12} = \frac{30 \bullet n_b \cdot k_b \cdot k_t \cdot d \cdot f_u}{E} \tag{13}$$

$$k_b = k_{b1} \text{ but } k_b \leq k_{b2} \tag{14}$$

$$k_{b1} = 0.25 \bullet \frac{e_b}{d} + 0.5 \text{ but } k_{b1} \leq 1.25 \tag{15}$$

$$k_{b2} = 0.25 \bullet \frac{p_b}{d} + 0.375 \text{ but } k_{b2} \leq 1.25 \tag{16}$$

$$k_t = 1.5 \bullet \frac{t_j}{d_{M16}} \text{ but } k_t \leq 2.5 \tag{17}$$

4.2. Analytical model of springs

The primary mechanical components governing the joint response were assembled into an analytical model, whose configuration is shown in Fig. 16. The overall rotational stiffness of the joint is obtained by combining the individual deformations of these components, as defined by their respective stiffness equations. These components are arranged in series and/or parallel, depending on their mechanical interaction within the joint.

4.3. Stiffness results

The analytical rotational stiffness and the experimental rotational stiffness are compared in Table 5, which also includes the ratio of tube width to tube thickness, denoted as the h/t ratio, for each joint to describe the wall slenderness. From the results, it can be inferred that increasing the thickness of the column leads to a higher initial rotational stiffness of the joint. Additionally, Table 5 presents the ratio of experimental to analytical rotational stiffness, showing a reasonable agreement with a mean value of 1.03 and a standard deviation of 0.06. As shown in Table 5, the accuracy of the analytical model does not exhibit a consistent trend with increasing h/t. Instead, discrepancies appear more strongly associated with connection configuration, particularly the number and arrangement of angle cleats that govern load transfer mechanism between the tube and base plate.

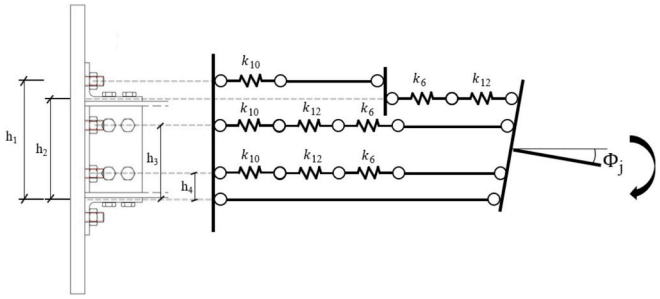

Fig. 16. Simplified spring model of the column-to-base plate joint based on the component method.

Table 5
Experimental rotational stiffness ($S_{j,EXP}$) and analytical rotational stiffness ($S_{j,an}$) of the column-to base plate joints.

Joint	h/t	$S_{j,EXP}$ [kNm/rad]	$S_{j,an}$ [kNm/rad]	$S_{j,an}$/ $S_{j,EXP}$
BM1	33	5661	5635	1,02
BM1-SA	33	3677	3176	1,16
BM2	25	5979	6225	0,98
BM2-SA	25	4391	4107	1,07
BM3	20	6924	6678	1,05
BM4	33	5181	5439	0,97
BM5	25	5792	6040	0,97
BM6	20	6554	6438	1,03

From the data shown, it can be inferred that joints with disconnected lateral angle cleats exhibit a noticeable drop in their rotational stiffness. When comparing the results with joints featuring four angle cleats, this drop was quantified as 35 % for the joint denoted BM1-SA and 27 % for the joint BM2-SA.

Furthermore, the joints formed by SHS-columns presented a higher initial stiffness than those formed by RHS-columns, which can be justified by the fact that the length of the top and seat angle cleats in the SHS-joints was 180 mm, while the length of the angle cleats in RHS-joints was 130 mm, determined by the tube width and clearance requirements.

Fig. 17 presents a comparison between the analytical and numerical (or experimental, when available) initial rotational stiffness values for the tested joints with four angle cleats, with dotted lines representing a ± 20 % deviation from the experimental results. The ratio $S_{j,NUM}$ / $S_{j,an}$ ranges from 1.03 to 1.24, with an average value of 1.11. Most data points align closely with the identity line, though predominantly positioned below it, reflecting a systematic underestimation of joint stiffness by the analytical model. Such deviations are modest when compared to the results obtained by other authors in literature [42–46] and may be indicative of the intrinsic simplifications adopted in the analytical model, which tend to yield conservative estimates of joint stiffness. Nevertheless, the analytical predictions exhibit a coherent trend across the full range of joint geometries and demonstrate an acceptable agreement with numerical results, suggesting the applicability of the component-based model for stiffness estimation in demountable column-to-base plate connections.

4.4. Joint classification by stiffness

The tested and numerically simulated column-to-base plate joints were classified according to the Eurocode 3 proposal for column bases.

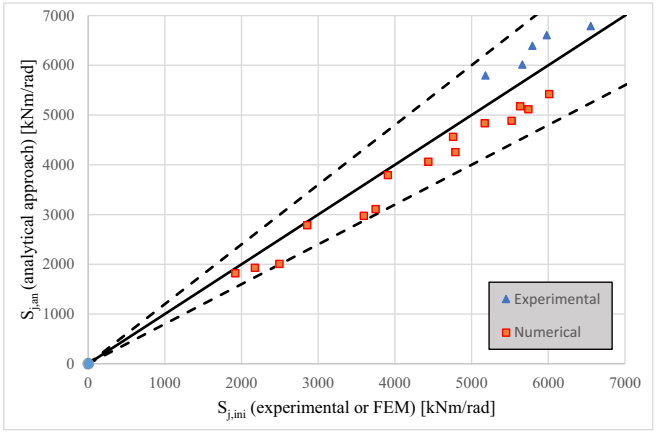

Fig. 17. Assessment of column-to-base plate stiffness analytical and numerical approach.

All joints were classified by stiffness considering a column length of 3 m.

Fig. 18 shows the relationship between the stiffness obtained in the tests $S_{j,exp}$ (or the stiffness obtained by numerical simulation for the numerically simulated joints, $S_{j,num}$) and the rigid boundary $S_{j,rigid}$ ($S_{j,rigid} = [7\cdot(2\lambda_0-1)\cdot E\cdot I_c/L_c]$) for columns with slenderness ratios between 0.5 and 3.93, for different column-base plate joint geometries. Values greater than one means joints classified as rigid when $0.5 < \lambda_0 < 3.93$. Negative values in the figure are associated with joints with slenderness ratios less than 0.5 ($\lambda_0 < 0.5$).

Therefore, based on the classification outlined by Eurocode, both the tested joints and the numerically simulated joints can be classified as rigid in non-sway frames.

5. Analytical model of resistance

The moment resistance of column-to-base plate joints under bending moments can be determined from the resistance of the weakest basic component, as specified in (18).

$$M_R = F_R \bullet z \tag{18}$$

Where F_R is the resistance of the weakest basic component of the joint and z is the lever arm of the joint.

The identified basic components were: several related with the studs (studs in tension, studs in shear, studs in combined tension and shear and punching shear of the studs in the base plate) and angle cleat in bending.

The failure mechanisms of the bolts connecting the beam flanges and angle cleats should be analysed as in other angle-cleated joints. However, since all joints under investigation were outfitted with oversized prestressed bolts, the investigation into potential slip, shear or bearing failures of these bolts could be excluded from this research.

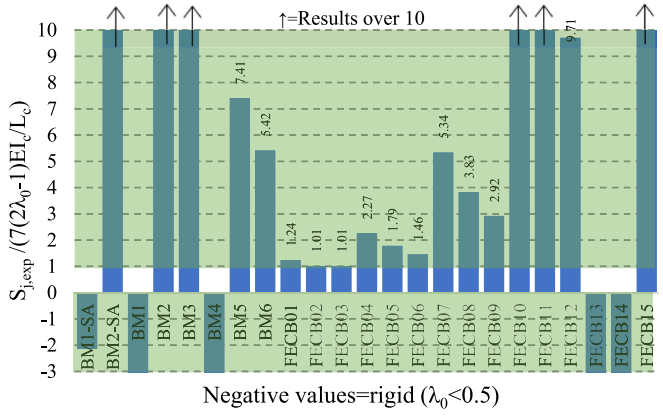

Fig. 18. Ratios between $S_{j,ini}$ and $S_{j,rigid}$ in the column-to-base plate joints classification by stiffness.

5.1. Resistance of welded studs

The resistance of the welded studs was determined by adapting the equations for bolts from Eurocode 3, Part 1.8. The studs were assessed under various loading conditions: tension, shear, combined tension and shear, and punching shear in the base plate.

The resistance of welded studs in tension, $F_{t,Rd}$, was calculated according to the eq. (19), where $f_{u,s}$ is the ultimate strength of the welded stud, A_s is the reduced area of the stud and γ_{M2} is the partial safety factor (in this study this factor has been assumed equal to one, while in the design standard the most common value is 1.25).

$$F_{t,Rd} = \frac{0.9 \bullet f_{u,s} \bullet A_s}{\gamma_{M2}} \tag{19}$$

The resistance of the frontal face of the column under punching shear, $B_{p,Rd}$, was calculated according to (20) where d_2 is the reduced diameter of the stud, t_{bp} is the thickness of the base plate, $f_{y,bp}$ is the yield stress of the base plate and γ_{M2} is the partial safety factor, assumed equal to 1.

$$B_{p,Rd} = \frac{0.6 \bullet \pi \bullet d_2 \bullet t_{bp\bullet} \bullet f_{y,bp}}{\gamma_{M2}} \tag{20}$$

The shear resistance of welded studs, denoted as $F_{v,Rd}$, was determined using eq. (21), where a_v represents a coefficient that varies depending on the class of the welded stud. For studs with shear plane passing through the threaded area, a_v equals 0.6 for class 8.8 and 0.5 for class 4.8. For cases where the shear plane passes through the unthreaded area, a_v is set to 0.6. Other parameters include $f_{u,s}$ for the ultimate strength of the welded stud, A_s for the reduced area of the stud, and γ_{M2} for the partial safety factor.

$$F_{v,Rd} = \frac{a_v \bullet f_{u,s} \bullet A_s}{\gamma_{M2}} \tag{21}$$

The resistance of welded studs under tension combined with shear was calculated following the eq. (22) where $F_{v,Ed}$ is the applied shear, $F_{v,Rd}$ is the shear resistance of the stud, $F_{t,Ed}$ is the applied force and $F_{t,Rd}$ is the tension resistance of the stud.

$$\frac{F_{v,Ed}}{F_{v,Rd}} + \frac{F_{t,Ed}}{1.4\,F_{t,Rd}} \le 1 \tag{22}$$

The resistance of welded studs has been determined by studying the four possible failures that may occur: tension, punching, shear, and combined tension with shear. However, since there are multiple studs-rows in tension, two joint moment resistance that may lead to stud failure were calculated in column-base plate joints. The first occurs when the most stressed stud row reaches the design stud strength. This joint moment resistance, $M_{R,L}$, is calculated assuming a proportional distribution of the loads of each stud-row with respect to its distance to the centre of compression, assuming it is located at half thickness of the large leg for the compressed angle cleat (See Fig. 19, left). This means that the deformation capacity of the stud rows is limited in such a way that the redistribution of forces due to yielding among the stud rows is not possible. This joint moment resistance can be calculated according to eq. (11), where $F_{t,Rd}$ is the stud resistance to tension and 'h_j' is the distance from the stud-row 'j' to the centre of compression.

$$M_{R,L} = \frac{F_{t,Rd}}{h_j}\sum h_j^2 \tag{23}$$

The second joint moment resistance, $M_{R,U}$, was calculated considering complete yielding of all rows of studs (See Fig. 19, right), meaning

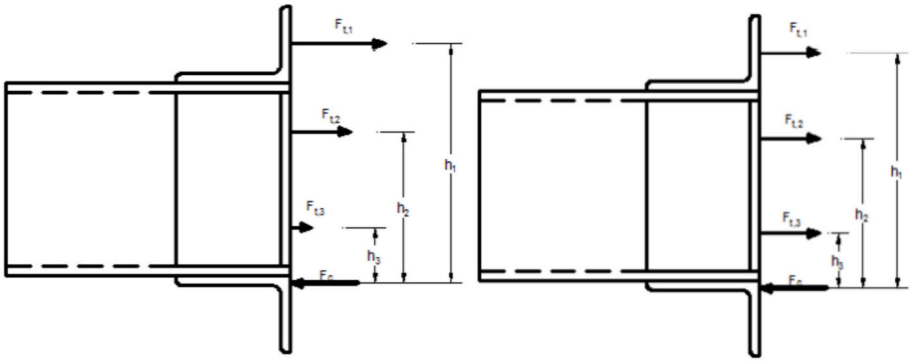

Fig. 19. Force distribution considering a proportional distribution between stud-rows (left) and force distribution assuming plastic deformation (right).

that all stud-rows have sufficient deformation capacity, so that the redistribution of forces among the stud-rows is complete. $M_{R,U}$ can be calculated according to eq. (24).

$$M_{R,U} = \sum F_{t,Rd} \bullet h_j \tag{24}$$

A case intermediate to those previously discussed involves incomplete or partial redistribution caused by insufficient deformation capacity in the outermost row of studs, which fail to reach the design resistance load. In other words, while some stud rows further from the compression centre fully yield, others do not reach this limit due to their limited deformation capacity.

5.2. Resistance of the flange cleat in bending

For bolted connections, an equivalent T-stub under tension can be utilized to depict the design resistance of the flange cleat under bending [53]. The failure of a T-stub flange can occur in three distinct modes: mode 1 involves complete yielding of the flange, mode 2 entails bolt failure alongside flange yielding, and mode 3 encompasses bolt failure alone.

The design resistance of the T-stub flange under mode 1 or complete yielding of the flange, $F_{T,1,Rd}$ was calculated by using the eq. (25) where $M_{pl,1Rd}$ is the moment when complete yielding of the flange occurs and m is obtained according to Fig. 20. The geometry-factor m considers the positions where the yielding of the flange can occur, that depending on the distance between the beam and the column, it could be in the long leg or in the short leg of the angle cleat. The detailed positions are described in Fig. 20.

$$F_{T,1,Rd} = \frac{4 \bullet M_{pl,1Rd}}{m} \tag{25}$$

$M_{pl,1,Rd}$ can be calculated with eq. (26) assuming a T-stub equivalent with an effective length $l_{eff,1}$ equal to 0.5 times the length of the angle cleat, in which t_l is the thickness of the angle cleat, $f_{y,l}$ is the yield stress of the angle cleat and γ_{M0} is the partial safety factor.

$$M_{pl,1,Rd} = \frac{\sum l_{eff,1} \bullet t_l^2 \bullet f_{y,l}}{4 \bullet \gamma_{M0}} \tag{26}$$

For a combined failure of the studs with yielding of the flange (mode 2), the design resistance $F_{T,2,Rd}$ was calculated with eq. (27), where $M_{pl,2,Rd}$ is the moment that produces the yielding of the flange, n is the distance between the stud-axis and the border of the leg of flange (see Fig. 20), $F_{t,Rd}$ is the resistance of studs and m is as defined in Fig. 20.

$$F_{T,2,Rd} = \frac{2 \bullet M_{pl,2,Rd} + n \sum F_{t,Rd}}{m + n} \tag{27}$$

$M_{pl,2,Rd}$ can be calculated with eq. (28) assuming a T-stub equivalent with an effective length $l_{eff,2}$ equal to 0.5 times the length of the angle cleat, in which t_l is the thickness of the angle cleat, $f_{y,l}$ is the yield stress of the angle cleat and γ_{M0} is the partial safety factor.

$$M_{pl,2,Rd} = \frac{\sum l_{eff,2} \bullet t_l^2 \bullet f_{y,l}}{4 \bullet \gamma_{M0}} \tag{28}$$

In case of a failure mode 3, the resistance of the welded studs $F_{T,3,Rd}$ was calculated with eq. (29) where $F_{t,Rd}$ is the resistance of the welded studs.

$$F_{T,3,Rd} = \sum F_{t,Rd} \tag{29}$$

Ultimately, the design tension resistance of the T-stub flange can be computed following eq. (18). Prying effects are implicitly considered when calculating the design tension resistance of $F_{T,1,Rd}$, $F_{T,2,Rd}$, and $F_{T,3,Rd}$.

$$F_{T,Rd} = \min\left(F_{T,1,Rd}, F_{T,2,Rd}, F_{T,3,Rd}\right) \tag{30}$$

5.3. Discussion

The analytical joint moment resistances, $M_{R,an}$, and associated failure modes for the tested specimens are presented in Table 6. The table also includes two columns with the analytical moment resistance leading to stud failure, under the condition where yielding is not achieved ($M_{R,L}$),

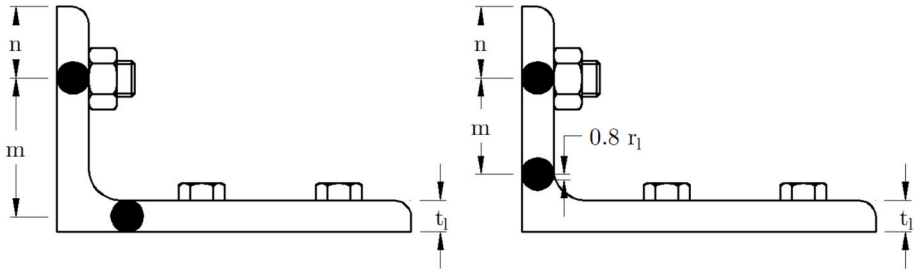

Fig. 20. Definition of the m-parameter, variable with the distance between the beam and the column. When the distance is higher than 0.4 t_l (left) and when the distance is lower or equal to 0.4 t_l (right)

as well as the moment resistance at which analytical stud failure occurs with complete yielding across all stud rows ($M_{R,U}$).

From the analytical results, it is observed that specimens with shorter upper and lower angle cleats (specimens BM4 to BM6), the first failure mode is due to the yielding of the angle cleat. In the remaining cases, the first observed failure mode is the breakage of the stud. Comparing experimental joint moment resistances with analytical ones, it is observed that for specimen BM6, the yielding of the angle cleat is analytically obtained at a moment of 68.2 kNm, while the stud failure (second observed failure mode) occurs between $M_{R,L} = 77.7$ kNm when no yielding is considered in any stud row, and $M_{R,U} = 101.6$ kNm when complete yielding is considered in all stud rows. Experimentally, after the flange yielding (See Fig. 21), the breakage of one of the studs located in the furthest tensioned stud row from the compression centre, was observed when a moment of $M_{R,EXP} = 78.0$ kNm was applied. This corresponds to a deviation of 0.5 % from the analytical estimation, taking the latter as $M_{R,L}$, and of 23.2 % taking the latter as $M_{R,U}$.

Regarding specimen BM3, the test concluded before fracture when reaching the maximum actuator displacement. This point corresponds to a moment of $M_{R,EXP} = 84.4$ kNm, which falls within the range where failure of the stud is expected to occur, as analytically derived resistant moments in the studs $M_{R,L} = 77.7$ kNm when yielding is considered in one stud rows, and $M_{R,U} = 101.6$ kNm, when complete yielding is considered in all stud rows.

For specimens BM1-SA and BM2-SA, $M_{R,U}$ coincides with $M_{R,L}$ since these specimens only feature one tensioned stud row, having disconnected the side angle cleats of the column faces. For the remaining specimens, they exhibit the same $M_{R,U}$ and the same $M_{R,L}$ because these moments solely depend on the separation of the stud rows, and such separation was kept constant across all samples.

In the last column of Table 6, plastic moment capacity of SHS and RHS profiles ($M_{R,0}$), calculated as the product of the plastic section modulus by the nominal yield strength, is presented. Comparing these results with the analytical joint moment resistance reveals predominantly partial strength joints based on moments alone. Nonetheless, the introduction of typical compressions in building columns would enhance joint strength, quickly transitioning these column-base plate connections to full strength.

The analytical moment resistance, $M_{R,an}$, and associated failure modes for numerically simulated column-base plate connections are presented in Table 7. Results indicate that due to shorter angle lengths, the joint failure mode is predominantly governed by the yielding of the angle cleat. The findings suggest that in these joints formed by tubes with a lower cross-section, studs with a smaller diameter could be used without compromising joint ductility. However, enhancing joint strength would entail increasing the thickness of the angle cleat. For instance, using 12-mm thickness angle cleats the resistance to yielding would increase from 29 % (specimen FEPB01) to 71 % (specimen FECB15). Nonetheless, this would come at the reduction of ductility, leading to non-compliance with the requirements outlined in [41] for achieving high ductility joints.

Table 6
Analytical results. Experimental moment resistance ($M_{R,EXP}$), analytical moment resistance ($M_{R,an}$), analytical failure modes, analytical moment resistance resulting in stud failure without stud yielding ($M_{R,L}$), analytical moment resistance resulting in stud yielding in all rows ($M_{R,U}$) and analytical moment resistance of the column ($M_{R,0}$).

Specimen	$M_{R,EXP}$ [kNm]	$M_{R,an}$ [kNm]	Analytical Failure mode	$M_{R,L}$ [kNm]	$M_{R,U}$ [kNm]	$M_{R,0}$ [kNm]
BM1	–	77.7	S (T)	77.7	101.6	90.8
BM1-SA	–	54.7	S (T)	54.7	54.7	90.8
BM2	–	77.7	S (T)	77.7	101.6	115.8
BM2-SA	–	54.7	S (T)	54.7	54.7	115.8
BM3	84.4	77.7	S (T)	77.7	101.6	139.7
BM4	–	68.0	C (mode 1)	77.7	101.6	74.5
BM5	–	67.8	C (mode 1)	77.7	101.6	94.6
BM6	78.0	68.2	C (mode 1)	77.7	101.6	113

Notation: S: stud, T: tension, C: angle cleat.

6. Conclusions

In this paper, the stiffness and the resistance of demountable bolted joints connecting hollow-section columns to the base plate has been studied through experimental testing, finite element models and simplified analytical models. In the analytical models, the basic components of the joint were identified, according with the component method, and their individual stiffness and resistance was determined allowing the full joint behaviour to be quantified. The analytical and numerical models were validated by comparison with the corresponding experimental results and later the models were extended to obtain the behaviour of other column-to base plate joint geometries suitable for application in low-rise and medium-rise residential steel structures.

From this research, the following conclusions can be outlined:

1. The analytical model based on the component method provides reasonably accurate estimations of the initial rotational stiffness. Comparisons with experimental data demonstrate good agreement, with analytical-to-experimental stiffness ratios ranging from 0.95 to 1.16 and a mean value of approximately 1.03.
2. When compared to numerical simulations, the analytical model exhibits a consistent underestimation of joint stiffness. The ratio $S_{j,NUM}$ / $S_{j,an}$ ranges from 1.03 to 1.24, with an average value of 1.11. This systematic deviation is moderate and indicates the conservative nature of the analytical formulation.
3. According to the stiffness classification provisions in Eurocode 3, all tested and simulated joints qualify as rigid connections for use in non-sway frames with typical column heights. This confirms the structural adequacy of the proposed demountable configuration under standard design assumptions.
4. Joints configured with only two angle cleats exhibit substantial reductions in initial stiffness—up to 35 %—compared to their four-cleat counterparts. This highlights the critical role of complete cleat configuration in maintaining structural performance.
5. Regression analyses reveal that the initial stiffness is not governed solely by the section's moment of inertia. The tube wall thickness exerts an independent structural influence, as confirmed by sparse and symbolic regression models, which retained wall thickness as a key predictor.
6. By normalizing the numerical stiffness $S_{j,NUM}$ with respect to I and scaling by t^2, all joint configurations collapse onto a single trend when plotted against the slenderness ratio h/t. This enables the definition of a generalized stiffness decay law based on wall slenderness, providing a scalable framework for estimating stiffness in geometrically similar connections.
7. The analytical model for joint moment resistance accurately identifies the governing failure modes—either angle cleat yielding or stud fracture—and provides design moment predictions with acceptable agreement, which are useful in preliminary design stages.

CRediT authorship contribution statement

Ismael García García: Writing – original draft, Software, Methodology, Investigation, Formal analysis, Data curation, Conceptualization. **Carlos López-Colina Pérez:** Writing – review & editing, Validation, Project administration, Methodology, Conceptualization. **Miguel Ángel Serrano López:** Writing – review & editing, Validation, Resources, Project administration, Methodology, Funding acquisition, Conceptualization. **Fernando López Gayarre:** Resources. **Antolín Lorenzana Ibán:** Resources.

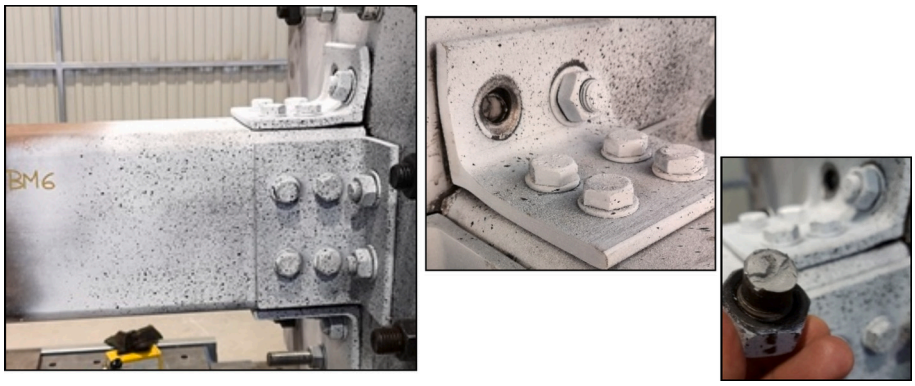

Fig. 21. Failure mode of specimen BM6. Left: specimen after the test. Centre: detail of the upper angle bracket. Right: detail of the stud after fracture.

Table 7
Analytical moment resistance ($M_{R,an}$) and failure modes in numerically simulated column-base plate connections.

Joint	$M_{R,an}$ [kNm]	Failure mode (an.)	$M_{R,L}$ [kNm]	$M_{R,U}$ [kNm]
FEPB01	19.6	C (mode 1)	49.7	65.9
FEPB02	19.6	C (mode 1)	49.7	65.9
FEPB03	19.6	C (mode 1)	49.7	65.9
FEPB04	27.2	C (mode 1)	57.5	74.8
FEPB05	27.2	C (mode 1)	57.5	74.8
FEPB06	27.2	C (mode 1)	57.5	74.8
FEPB07	36.2	C (mode 1)	65.5	83.7
FEPB08	36.2	C (mode 1)	65.5	83.7
FEPB09	36.2	C (mode 1)	65.5	83.7
FEPB10	43.9	C (mode 1)	71.7	90.4
FEPB11	43.9	C (mode 1)	71.7	90.4
FEPB12	43.9	C (mode 1)	71.7	90.4
FEPB13	46.6	C (mode 1)	73.7	92.6
FEPB14	46.6	C (mode 1)	73.7	92.6
FEPB15	46.6	C (mode 1)	73.7	92.6

Notation: C: angle cleat.

Declaration of competing interest

The authors declare that they have no known competing financial interests or personal relationships that could have appeared to influence the work reported in this paper.

Acknowledgements

The authors would like to acknowledge the financial support provided by the Spanish State Research Agency (AEI) through projects PID2021-126636NB-I00, BIA2017-83467-P and pre-doctoral grant PRE2018-084273. They would also like to thank the TESCAH Research Group from the University of Oviedo for their support.

Data availability

Data will be made available on request.

References

[1] L. Pérez-Lombard, J. Ortiz, C. Pout, A review on buildings energy consumption information, Energ. Buildings 40 (2008) 394–398, https://doi.org/10.1016/j.enbuild.2007.03.007.
[2] M. Marzouk, N. Elshaboury, Science mapping analysis of embodied energy in the construction industry, Energy Rep. 8 (2022) 1362–1376, https://doi.org/10.1016/j.egyr.2021.12.049.
[3] M. Sillanpää, C. Ncibi, The circular economy: Case studies about the transition from the linear economy, 2019, https://doi.org/10.1016/C2017-0-02916-6.
[4] M. Norouzi, M. Chàfer, L.F. Cabeza, L. Jiménez, D. Boer, Circular economy in the building and construction sector: a scientific evolution analysis, J. Build. Eng. 44 (2021) 102704, https://doi.org/10.1016/j.jobe.2021.102704.
[5] E. Hertwich, R. Lifset, S. Pauliuk, N. Heeren, S. Ali, Q. Tu, et al., Resource efficiency and climate change: material efficiency strategies for a low-carbon, Future (2021), https://doi.org/10.5281/zenodo.5245528.
[6] T. Harjula, B. Rapoza, W.A. Knight, G. Boothroyd, Design for Disassembly and the environment, CIRP Ann. Manuf. Technol. 45 (1996) 109–114, https://doi.org/10.1016/S0007-8506(07)63027-3.
[7] F.C. Rios, W.K. Chong, D. Grau, Design for disassembly and deconstruction - challenges and opportunities, Procedia Eng. 118 (2015) 1296–1304, https://doi.org/10.1016/j.proeng.2015.08.485.
[8] P. Crowther, Design for disassembly – themes and principles, Environ. Des. Guide. (2005) 1–7. http://www.jstor.org/stable/26149108.
[9] L.A. Akanbi, L.O. Oyedele, O.O. Akinade, A.O. Ajayi, M.D. Delgado, et al., Salvaging building materials in a circular economy: a BIM-based whole-life performance estimator, Resour. Conserv. Recycl. 129 (2018) 175–186, https://doi.org/10.1016/j.resconrec.2017.10.026.
[10] S. Kitayama, O. Iuorio, Disassembly and reuse of structural members in steel-framed buildings: state-of-the-art review of connection systems and future research trends, J. Archit. Eng. 29 (2023), https://doi.org/10.1061/JAEIED.AEENG-1615.
[11] E. Commission, J.R. Centre, M. Cordella, S. Donatello, M. Traverso, et al., A common EU framework of core sustainability indicators for office and residential buildings – part 3, how to make performance assessments using level(s), Publications Office (2017), https://doi.org/10.2760/95143.
[12] C. Vandervaeren, W. Galle, A. Stephan, N. De Temmerman, More than the sum of its parts: considering interdependencies in the life cycle material flow and environmental assessment of demountable buildings, Resour. Conserv. Recycl. 177 (2022) 106001, https://doi.org/10.1016/j.resconrec.2021.106001.
[13] D. Ridley-Ellis, Rectangular Hollow Sections with Circular Web Openings. http://researchrepository.napier.ac.uk/id/eprint/8229, 2000.
[14] C. Málaga-Chuquitaype, A.Y. Elghazouli, Component-based mechanical models for blind-bolted angle connections, Eng. Struct. (2010), https://doi.org/10.1016/j.engstruct.2010.05.024.
[15] A.Y. Elghazouli, C. Málaga-Chuquitaype, J.M. Castro, A.H. Orton, Experimental monotonic and cyclic behaviour of blind-bolted angle connections, Eng. Struct. (2009), https://doi.org/10.1016/j.engstruct.2009.05.021.
[16] H.-T. Thai, T.P. Vo, T.-K. Nguyen, C.H. Pham, Explicit simulation of bolted endplate composite beam-to-CFST column connections, Thin-Walled Struct. 119 (2017) 749–759, https://doi.org/10.1016/j.tws.2017.07.013.
[17] L. Yang, L. Peng, H. Ban, Experimental study on demountable and reusable steel beam-to-column joints with bolted-pinned connections, J. Constr. Steel Res. 214 (2024) 108450, https://doi.org/10.1016/j.jcsr.2023.108450.
[18] H. Wang, B. Zhang, H. Qian, J. Liu, B. An, F. Fan, Experimental and numerical studies of a new prefabricated steel frame joint without field-welding: design and static performance, Thin-Walled Struct. 159 (2021) 107271, https://doi.org/10.1016/j.tws.2020.107271.
[19] Y. Liu, C. Málaga-Chuquitaype, A.Y. Elghazouli, Response and component characterisation of semi-rigid connections to tubular columns under axial loads, Eng. Struct. 41 (2012) 510–532, https://doi.org/10.1016/j.engstruct.2012.03.061.
[20] L.-H. Han, W.-D. Wang, X.-L. Zhao, Behaviour of steel beam to concrete-filled SHS column frames: finite element model and verifications, Eng. Struct. 30 (2008) 1647–1658, https://doi.org/10.1016/j.engstruct.2007.10.018.
[21] R. Maquoi, X. Naveau, Beam-Column Welded Stud Connections, CIDET 5AG 83/5, 1983.
[22] R. Maquoi, X. Naveau, J. Rondal, Beam-column welded stud connections, J. Constr. Steel Res. 4 (1984) 3–26, https://doi.org/10.1016/0143-974X(84)90032-4.
[23] D. Vandegans, Liaison entre poutres métalliques et colonnes en profils creux remplis de béton, basée sur la technique du goujonnage (goujons filetés), 1995.
[24] D. Vandegans, Use of threaded studs in joints between I-beam and RHS-column, in: IABSE (Ed.), Istanbul Colloquium on Semi-Rigid Connections, Zürich, Switzerland, 1996, pp. 53–62.
[25] D. Vandegans, J. Janss, Connection between steel beams and concrete filled R.H.S. Based on the stud technique (threaded stud), Connections in Steel Struct. III (1996) 67–76, https://doi.org/10.1016/B978-008042821-5/50066-3.
[26] L.C. Neves, L.S. da Silva, P.C.G. da S. Vellasco, Experimental behaviour of end plate I-beam to concrete-filled rectangular hollow section column joints, Adv. Steel

Struct. (ICASS '02) (2002) 253–260, https://doi.org/10.1016/B978-008044017-0/50029-9.
[27] M.A. Serrano-López, C. López-Colina, I. García-García, F. López-Gayarre, Semi-rigid beam-column and column-base joints using welded threaded studs, in: 11th Int. Symp. Steel Struct. (ISSS−2021), 2021, pp. 450–453.
[28] M.A. Serrano-López, C. López-Colina, I. García-García, M. Lozano, F. López-Gayarre, Removable and Efficient Welded Stud Connections in Common Applications. Final report of project 5CF-1/21, in: CIDECT, 2021.
[29] R. Hasan, N. Kishi, W.F. Chen, M. Komuro, Evaluation of rigidity of extended end-plate connections, J. Struct. Eng. 123 (1997) 1595–1602, https://doi.org/10.1061/(ASCE)0733-9445(1997)123:12(1595).
[30] N. Kishi, M. Komuro, W.F. Chen, Four-parameter power model for M-θ R curves of end-plate connections, in: Fifth Int. Workshop Connections in Steel Struct., Amsterdam, 2004, pp. 99–110.
[31] J.D. Gao, H.X. Yuan, X.X. Du, X.B. Hu, M. Theofanous, Structural behaviour of stainless steel double extended end-plate beam-to-column joints under monotonic loading, Thin-Walled Struct. 151 (2020) 106743, https://doi.org/10.1016/j.tws.2020.106743.
[32] C. Faella, V. Piluso, G. Rizzano, A new method to design extended end plate connections and semirigid braced frames, J. Constr. Steel Res. 41 (1997) 61–91, https://doi.org/10.1016/S0143-974X(97)00001-1.
[33] N. Kishi, W. Chen, Moment-rotation relations of semirigid connections with angles, J. Struct. Eng. 116 (1990) 1813–1834, https://doi.org/10.1061/(ASCE)0733-9445(1990)116:7(1813).
[34] C. Faella, V. Piluso, G. Rizzano, Experimental analysis of bolted connections: snug vs. preloaded bolts, J. Struct. Eng. (1998) 765–774.
[35] C. Faella, V. Piluso, G. Rizzano, Rotational stiffness prediction of flange and web angle connections with preloaded bolts, in: Ital. Conf. Steel Constr., Ancona, 1997.
[36] J.P. Jaspart, R. Maquoi, Effect of bolt preloading on joint behaviour, in: Kounadis (Ed.), Steel Struct., Eurosteel '95, Balkema, 1995.
[37] X. Chen, G. Shi, Experimental study of end-plate joints with box columns, J. Constr. Steel Res. 143 (2018) 307–319, https://doi.org/10.1016/j.jcsr.2017.12.029.
[38] Z. Tao, W. Li, B.-L. Shi, L.-H. Han, Behaviour of bolted end-plate connections to concrete-filled steel columns, J. Constr. Steel Res. 134 (2017) 194–208, https://doi.org/10.1016/j.jcsr.2017.04.002.
[39] J. Wang, L. Chen, Experimental investigation of extended end plate joints to concrete-filled steel tubular columns, J. Constr. Steel Res. 79 (2012) 56–70, https://doi.org/10.1016/j.jcsr.2012.07.016.
[40] I. García, M.A. Serrano, C. López-Colina, F.L. Gayarre, The stiffness of beam-to-RHS joints with welded studs, J. Build. Eng. 70 (2023) 106340, https://doi.org/10.1016/j.jobe.2023.106340.
[41] I. García, M.A. Serrano, C. López-Colina, F.L. Gayarre, The strength of beam-to-RHS joints with welded studs, J. Build. Eng. 76 (2023) 107203, https://doi.org/10.1016/j.jobe.2023.107203.
[42] A.M.G. Coelho, F.S.K. Bijlaard, Behaviour of high strength steel moment joints, Heron 55 (2010) 1–32.
[43] Z. Kong, S. Hong, Q.-V. Vu, X. Cao, S.-E. Kim, B. Yu, New equations for predicting initial stiffness and ultimate moment of flush end-plate connections, J. Constr. Steel Res. 175 (2020) 106336, https://doi.org/10.1016/j.jcsr.2020.106336.
[44] F. Kavoura, B. Gencturk, M. Dawood, Evaluation of existing provisions for design of "pinned" column base-plate connections, J. Constr. Steel Res. 148 (2018) 233–250, https://doi.org/10.1016/j.jcsr.2018.05.030.
[45] T. Lin, Z. Wang, F. Hu, P. Wang, Finite-element analysis of high-strength steel extended end-plate connections under cyclic loading, Materials 15 (2022) 2912, https://doi.org/10.3390/ma15082912.
[46] Y. Song, B. Uy, Effect of bolt preloading on rotational stiffness of stainless steel end-plate connections, Steel Compos. Struct. 48 (2023) 547–564, https://doi.org/10.12989/scs.2023.48.5.547.
[47] M.A. Serrano-López, C. López-Colina, Y.C. Wang, M. Lozano, I. García, F. L. Gayarre, An experimental study of I beam-RHS column demountable joints with welded studs, J. Constr. Steel Res. (2021), https://doi.org/10.1016/j.jcsr.2021.106651.
[48] O.S. Bursi, J.P. Jaspart, Basic issues in the finite element simulation of extended end plate connections, Comput. Struct. 69 (1998) 361–382, https://doi.org/10.1016/S0045-7949(98)00136-9.
[49] T. Wanzek, N. Gebbeken, Numerical aspects for the simulation of end plate connections, in: numerical simulation of semi-rigid connections by the finite element method, COST C1 (1999) 13–31.
[50] A.M. Citipitioglu, R.M. Haj-Ali, D.W. White, Refined 3D finite element modeling of partially-restrained connections including slip, J. Constr. Steel Res. 58 (2002) 995–1013, https://doi.org/10.1016/S0143-974X(01)00087-6.
[51] F. Pedregosa, G. Varoquaux, A. Gramfort, V. Michel, B. Thirion, et al., Scikit-learn: machine learning in python, J. Mach. Learn. Res. 12 (2011) 2825–2830.
[52] M. Cranmer, Interpretable machine learning for science with PySR and SymbolicRegression.jl. https://arxiv.org/abs/2305.01582, 2023.
[53] EN 1993−1-8, Design of steel structures - Part 1–8: Design of joints, Eurocode 3, 2005.
[54] C. Faella, V. Piluso, G. Rizzano, Structural Steel Semirigid Connections: Theory, Design, and Software, 1st ed., CRC Press, 1999.